# A facile one-pot preparation of $Bi_2O_2CO_3$/g-$C_3N_4$ composites with enhanced photocatalytic activity

Yongzheng Duan, Haibo Yao, Jing Li, Xili Shang, Dongmei Jia and Changhai Li

## ABSTRACT

$Bi_2O_2CO_3$ modified graphitic carbon nitride (g-$C_3N_4$) nanosheets were prepared by a simple one-pot synthetic strategy. In the presence of ammonium nitrate, different mass ratios of bismuth nitrate/melamine were used to fabricate these catalysts, which were characterized by X-ray diffraction (XRD), $N_2$-physisorption, Fourier transform infrared spectroscopy (FT-IR), transmission electron microscopy (TEM), X-ray photoelectron spectroscopy (XPS), UV-vis analysis, and photoluminescence (PL). The catalytic properties of composites were evaluated by photodegrading tetracycline hydrochloride (TC) under visible light irradiation. Among these catalysts, $Bi_2O_2CO_3$(1.5)/g-$C_3N_4$ showed the highest catalytic activity, which was more than 16 times greater than the pristine g-$C_3N_4$ material. The improved photocatalytic properties of $Bi_2O_2CO_3$/g-$C_3N_4$ may be due to the formation of a heterojunction between $Bi_2O_2CO_3$ and g-$C_3N_4$, leading to the effective separation of photo-induced carriers and the enhanced absorption of visible light. Furthermore, the $Bi_2O_2CO_3$/g-$C_3N_4$ composites had considerable catalytic stability, which was a key element for their potential applications.

**Key words** | $Bi_2O_2CO_3$, graphitic carbon nitride, nanosheet, photocatalytic

**Yongzheng Duan**
**Haibo Yao**
**Jing Li**
**Xili Shang** (corresponding author)
**Dongmei Jia**
**Changhai Li**
Department of Chemical Engineering and Safety,
Binzhou University,
Binzhou 256603,
China
and
Engineering Research Center for Wastewater Resource of Shandong Province,
Binzhou 256603,
China
E-mail: *xilishang@bzu.edu.cn*

## INTRODUCTION

Nowadays, water pollution has become one of the most severe environmental problems, which results in adverse effects on the ecological environment and human survival (Duan & Shen 2017; Ma *et al.* 2017a, 2017b; Rong *et al.* 2017). Industrial chemicals, dyes, pesticides and pharmaceuticals are the main pollutants of concern in wastewater owing to their high toxicity and hardly degradable properties. Among these efficient, green and safe purification techniques, the photocatalytic process has been regarded as the most promising solution, due to its potential to degrade a wide range of organic pollutants into nontoxic compounds under facile conditions (Jiang *et al.* 2013; Bai *et al.* 2017; Zheng & Jiao 2017). In this process, to make full use of the solar energy, a photocatalyst with a band gap lower than about 3.0 eV is desired (Akhundi & Habibi-Yangjeh 2017; Duan *et al.* 2018). Yet conventional photocatalysts such as $TiO_2$ and ZnO can almost absorb ultraviolet light, leading to poor photocatalytic properties under visible light illumination.

Recently, graphitic carbon nitride (g-$C_3N_4$) has been widely investigated, and has proven to be a promising metal-free visible light-driven photocatalyst, due to its low cost, high stability, great optical features, and ability to combine with different semiconductors (Wang *et al.* 2009; Wu *et al.* 2015). Nonetheless, the photocatalytic activity of bulk g-$C_3N_4$ is not high enough, owing to its low surface area, poor optical absorption from visible light, and fast charge-carrier recombination (Mamba & Mishra 2016; Wang *et al.* 2016).

In photocatalysis, the semiconductor nanosheet has been regarded as an interesting structure for its large surface area, which provides abundant active sites and ultrathin thickness, increasing the lifetime of photogenerated carriers. In general, thermal oxidation etching and ultrasonication-assisted liquid exfoliation are two common approaches to prepare g-$C_3N_4$ nanosheets from the bulk powders (Zhang *et al.* 2012, 2015a, 2015b; Chen *et al.* 2014; Lin *et al.* 2015). However, the former generates abundant interface defects and the latter has rather low yield. In recent times, a facial 'bottom-top' route has been reported to fabricate ultrathin g-$C_3N_4$ sheets, using a chemical blowing approach (Yan *et al.* 2016; Luo *et al.* 2017).

It is well known that combining g-$C_3N_4$ with other semiconductors is a valid method for suppressing the

doi: 10.2166/wst.2019.146

recombination of photogenerated carriers and improving photocatalytic performance. Bismuth subcarbonate ($Bi_2O_2CO_3$) with a band gap varying from 2.8 to 3.5 eV is a strong candidate due to its good photocatalytic performance and low mammalian toxicity for medicine treatment (Liang *et al.* 2014). $BiO_2CO_3$/g-C3N4 heterojunction catalyst can promote photogenerated electron-holes pairs' separation, and thus high catalytic efficiency is obtained (Tian *et al.* 2014; Xiong *et al.* 2014; Zhang *et al.* 2015a, 2015b; Ma *et al.* 2017a, 2017b). Unfortunately, all these catalysts have been prepared by multiple step procedures with long operation periods.

In this reported work, $Bi_2O_2CO_3$ modified graphitic carbon nitride (g-$C_3N_4$) nanosheets have been fabricated by the chemical blowing route. This composite material has been synthesized by thermal condensation of melamine and bismuth nitrate in the presence of ammonium nitrate. The visible light-driven photocatalytic degradation of tetracycline hydrochloride (TC) for $Bi_2O_2CO_3$/g-$C_3N_4$ has been carefully evaluated and found to be obviously enhanced in contrast to the pristine g-$C_3N_4$ material. In view of the ease of preparation and excellent performance, $Bi_2O_2CO_3$/g-$C_3N_4$ can be a promising and competitive visible light-induced photocatalyst in the area of environmental remediation.

## EXPERIMENTAL SECTION

### Materials

All chemicals were reagent grade and used directly without any further purification. Melamine, bismuth nitrate and ammonium nitrate have been purchased from Sinopharm Chemical Reagent Co. Ltd, China.

### Materials synthesis

The $Bi_2O_2CO_3$/g-$C_3N_4$ samples were prepared from the thermal condensation of melamine and bismuth nitrate in the presence of $NH_4NO_3$. In a typical synthesis, a mixture of 3.0 g of melamine and 0.45 g of ammonium nitrate was uniformly mixed with a specified amount of bismuth nitrate, and placed in a covered alumina crucible. The crucible was then heated in static air to 550 °C at a heating rate of 5 °C/min and held for 2 h. The synthesized catalyst was ground into a powder for further study. The catalysts used in this research were abbreviated as BiOC(x)/g-CN, where x represents the amount of $Bi_2O_2CO_3$ in the catalyst (wt %). A pure g-$C_3N_4$ sample was also obtained by the same conditions without adding bismuth nitrate.

### Characterizations

High resolution transmission electron microscopic images were taken using a JOEL JEM-2100 microscope equipped with energy dispersive spectroscopy. The nitrogen adsorption-desorption isotherms of different samples were determined at 77 K on a Micromeritics ASAP 2000 apparatus. The pore structural data were calculated by the BJH (Barrett-Joyner-Halenda) method of adsorption. The metallic contents were obtained by X-ray fluorescence (XRF) measurements on an ARL9800 XRF. X-ray diffraction (XRD) patterns of samples were monitored on a Philips PW 3830 diffractometer using Cu Ka radiation ($\lambda = 1.5418$ Å). The scattering angle was between 10° and 70° at an interval of 0.02°. Fourier transform infrared spectra (FT-IR) were recorded on a Bruker Tensor 27. X-ray photoelectron spectroscopy (XPS) measurements were carried out on a Thermo ESCALAB 250 instrument (USA) using nonmonochromatic Al K$\alpha$ (h$\nu = 1486.6$ eV) radiation. Diffuse reflectance spectra were recorded using a Cary 100 Bio UV–visible spectrophotometer with Harrick Scientific accessory. The photoluminescence (PL) spectra were measured using a FLS-920 spectrometer (Edinburgh Instruments) with excitation wavelength of 310 nm.

### Photocatalytic tests

In the experimental setup, a 300 W Xe-arc lamp was utilized as a light source and a 420 nm cut-off filter ($\lambda > 420$ nm) was used to provide only visible light irradiation. About 50 mg catalyst was added to 50 ml TC aqueous solution with a concentration of $1 \times 10^{-4}$ M. Before being irradiated, the suspensions were magnetically stirred in the dark for 1 h to reach the adsorption-desorption equilibrium between photocatalysts and TC. Then the solution was exposed to visible light irradiation under magnetic stirring. Samples were then taken out regularly from the reactor, and immediately centrifuged (4,000 rpm) to remove particles. The degradation of TC was monitored by checking the absorbance at 357 nm using a Shimadzu UV-2550 UV-vis spectrometer. The photocatalytic degradation efficiency was calculated by the following equation:

$$\text{Degradation efficiency } (\%) = (C_o - C_t)/C_o \times 100\%$$

where t is the reaction time, $C_o$ and $C_t$ represent the concentration of TC initially and at irradiation time t.

To verify the stability of the catalyst, repetitive use of BiOC(1.5)/g-CN for TC photocatalytic degradation was

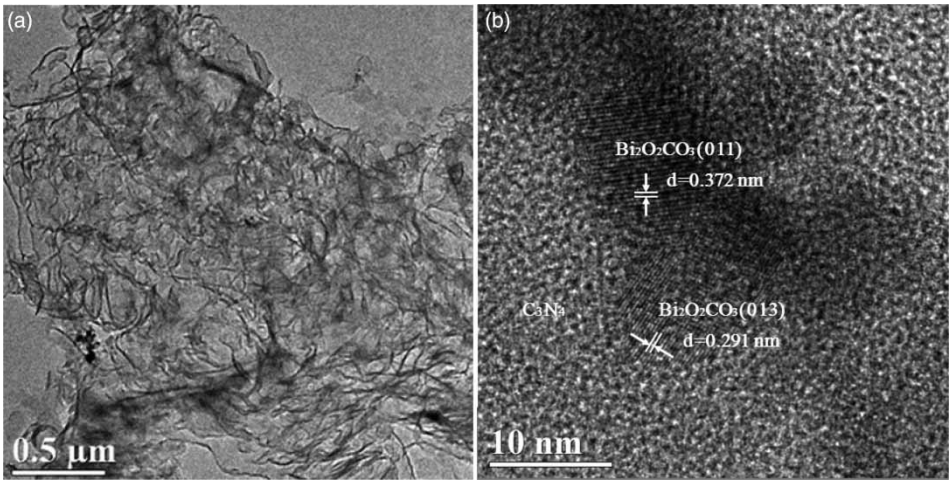


**Figure 1** | TEM images (a) and HR-TEM image (b) of BiOC(1.5)/g-CN.

carried out. In each experiment, the catalyst was reused after washing by simple filtration followed by ultrasonic cleaning with a mixture of 30% ethanol in water, then dried at 120 °C for 5 h.

## RESULTS AND DISCUSSION

The 3D bulky g-$C_3N_4$ is stacked by 2D carbon nitride layers which have been thermally condensed from melamine molecules. By introducing ammonium nitrate and bismuth nitrate into the preparation process, melamine is polymerized around $NH_4NO_3$ and $Bi(NO_3)_3$ particles, and chemical blowing gas liberated from the pyrolysis of bismuth nitrate and ammonium nitrate can blow the polymerized g-$C_3N_4$ sheets separately. Meanwhile, a solid $Bi_2O_2CO_3$ product (which was formed by $Bi_2O_3$ in the presence of chemical blowing gas) appears on these g-$C_3N_4$ sheets. Figure 1(a) shows that the BiOC(1.5)/g-CN sample possesses a two-dimensional irregular foliated nanosheet structure. From the high-resolution transmission electron microscopy (TEM) image (Figure 1(b)), it can also be observed that the bismuth species are well dispersed over the g-$C_3N_4$ nanosheets. The distinct lattice fringe spacing d of 0.372 nm and 0.291 nm can be ascribed to the (011) and (013) planes of tetragonal phase $Bi_2O_2CO_3$, respectively (Ma *et al.* 2017a, 2017b). Moreover, an interconnected fine morphology can be observed, implying that the BiOC/g-CN heterojunction has been formed in the composite catalyst.

The nitrogen adsorption-desorption isotherms of different samples are exhibited in Figure 2(a), and the detailed textural characteristics are provided in Table 1. These samples have Type IIb isotherms, indicating that they all possess a sheet–like structure (Panneri *et al.* 2016). It is clear that, compared with g-CN, each BiOC/g-CN sample has a larger Brunauer-Emmett-Teller (BET) surface

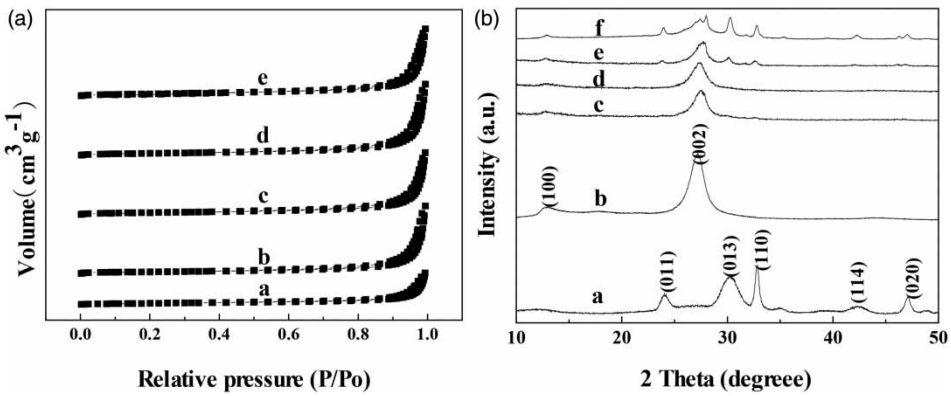


**Figure 2** | (a) Nitrogen adsorption-desorption isotherms of different samples: (a) g-CN, (b) BiOC(0.5)/g-CN, (c) BiOC (1.0)/g-CN, (d) BiOC(1.5)/g-CN, (e) BiOC(2.0)/g-CN; (b) XRD patterns of different samples: (a) $Bi_2O_2CO_3$, (b) g-CN, (c) BiOC(0.5)/g-CN, (d) BiOC(1.0)/g-CN, (e) BiOC(1.5)/g-CN, (f) BiOC (2.0)/g-CN.

**Table 1** | Properties of g-$C_3N_4$ and the various subject catalysts

| Sample | Bi[a] (wt %) | $S^b_{BET}$ ($m^2$/g) | Pore volume[c] ($cm^3$/g) |
|---|---|---|---|
| g-$C_3N_4$ | _ | 12.40 | 0.08 |
| BiOC(0.5)/g-$C_3N_4$ | 0.41 | 22.01 | 0.16 |
| BiOC(1.0)/g-$C_3N_4$ | 0.79 | 24.90 | 0.18 |
| BiOC(1.5)/g-$C_3N_4$ | 1.25 | 26.01 | 0.19 |
| BiOC(2.0)/g-$C_3N_4$ | 1.67 | 22.65 | 0.17 |

[a]Results from XRF analysis.
[b]BET method.
[c]Calculated at P/Po = 0.95.

area, which is favorable for its catalytic application. The XRD pattern analysis of the synthesized samples is exhibited in Figure 2(c). The diffraction peak at 27.7° of g-CN reflects the characteristic interlayer stacking reflection of conjugated aromatic systems, which can be indexed as (002) diffraction planes, while the (100) diffraction peak sited at 13.1° corresponds to the interplanar structural packing (Dong *et al.* 2013). For BiOC/g-CN composites, the (002) and (100) diffraction peaks that belong to g-CN are distinctly weakened and broadened, implying that the stacking structure of g-CN has been broken partly owing to the intercalation of $Bi_2O_2CO_3$ species and the g-CN layer being thinner (Shinde *et al.* 2016). It also can be observed that, when the content of $Bi_2O_2CO_3$ is less than 1.5 wt %, the peaks corresponding to $Bi_2O_2CO_3$ are not found, suggesting that bismuth species are evenly dispersed on the surface of g-CN sheets. And with an increase in the amount of bismuth species, the diffraction peaks of tetragonal phase $Bi_2O_2CO_3$

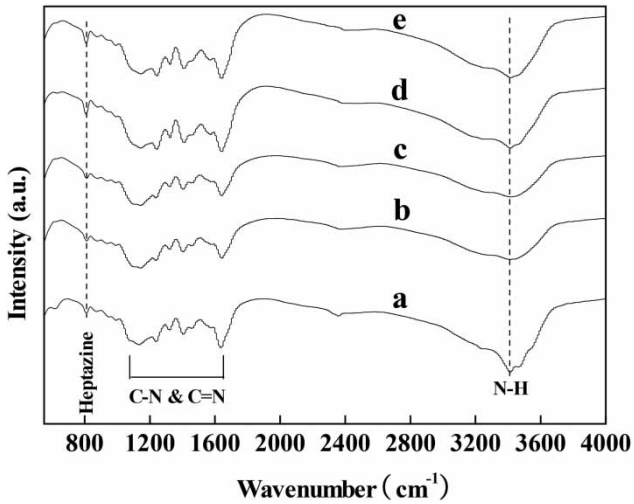


**Figure 3** | FT-IR spectra of different samples: (a) g-CN, (b) BOC(0.5)/g-CN, (c) BiOC(1.0)/g-CN, (d) BiOC(1.5)/g-CN, (e) BiOC(2.0)/g-CN.

can be observed. The FT-IR spectra of g-CN and different catalysts are shown in Figure 3. For g-CN, several bands between 1,100–1,650 $cm^{-1}$ are attributed to the stretching vibrations of C-N and C = N, and the band at 806 $cm^{-1}$ is associated with the breathing modes of triazine rings (Dong *et al.* 2011; Li *et al.* 2014). As for BiOC/g-CN composites, the spectra display clear vibration modes of g-CN, which may be due to the weak vibration mode of $Bi_2O_2CO_3$ and the strong IR response of g-CN (Li *et al.* 2015).

The surface elemental composition of BiOC/g-CN was investigated by XPS measurement. The XPS survey spectrum of BiOC(1.5)/g-CN shown in Figure 4(a) exhibits the presence of carbon, nitrogen, bismuth and oxygen. The high-resolution spectrum of Bi 4f (Figure 4(b)) shows two distinct peaks at 159.1 and 164.3 eV, attributed to Bi $4f_{7/2}$ and Bi $4f_{5/2}$ of BiOC(1.5)/g-CN. The conventional peaks of pure $Bi_2O_2CO_3$ can be observed at 158.2 and 163.4 eV, as reported (Zhang *et al.* 2015a, 2015b). Such a shift is attributed to the change of chemical environment caused by the interaction between $Bi_2O_2CO_3$ and g-$C_3N_4$ (Yang *et al.* 2014). The C 1 s spectrum (Figure 4(c)) shows two dominant peaks around 284.1 eV and 287.6 eV, corresponding to C = N $sp^2$ bonds and the overlapping of $sp^2$ C atoms in g-$C_3N_4$ and carbonate in $Bi_2O_2CO_3$ (Zhang *et al.* 2015a, 2015b). Figure 4(d) exhibits the N 1s XPS spectrum of BiOC(1.5)/g-CN, which can be deconvoluted into three peaks at 397.8, 398.5, and 400.1 eV, indexed as the C-N $sp^3$ bonds, C = N $sp^2$ bonds, and the interaction of g-CN sheets with $Bi_2O_2CO_3$, respectively (Jiang *et al.* 2016). The high-resolution spectrum of O 1s (Figure 4(e)) displays two distinct peaks at 530.8 and 533.4 eV. The peak sited at 530.8 eV is assigned to $O^{2-}$ ions in the Bi–O bonds, whereas the peak at 533.4 eV is attributed to the chemisorbed oxygen due to hydroxyl radicals.

Figure 5(a) exhibits the UV-vis reflectance spectra of g-CN,$Bi_2O_2CO_3$, and BiOC/g-CN composites with different bismuth concentrations. For the sake of clarity, only the spectra of BiOC(0.5)/g-CN, BiOC(1.5)/g-CN and BiOC(2.0)/g-CN samples are present. g-CN holds an absorption edge at around 475 nm in the visible range. Interestingly, all these BiOC/g-CN composites show improved absorption intensities over g-CN, indicating loading with $Bi_2O_2CO_3$ is conducive to the adsorption of the photons. By comparison with g-CN, there are obvious red shifts of the band edges of the BiOC/g-CN composites. Based on the higher absorption intensity, the improved photocatalytic performance of the BiOC/g-CN heterojunction could be anticipated under visible light illumination. The band gap energy of a semiconductor can be calculated

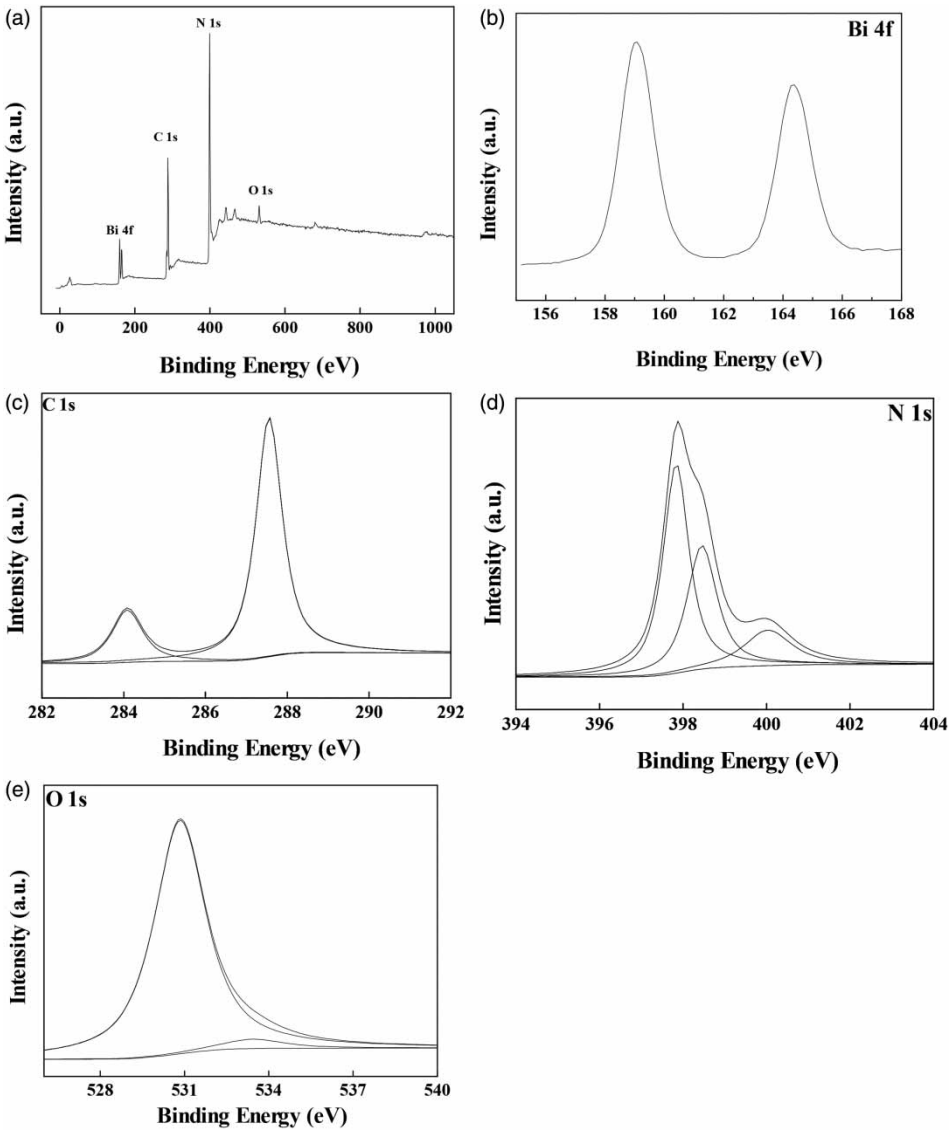


**Figure 4** | XPS spectra of BiOC(1.5)/g-CN catalyst: (a) full spectra, (b) Bi 4f, (c) C 1s, (d) N 1s, and (e) O 1s.

according to the formula: $(\alpha h\nu)^{1/n} = A(h\nu\text{-}Eg)$, where $\alpha$, h, $\nu$, Eg and A, are, respectively, the absorption coefficient, Planck constant, light frequency, band gap energy, and a constant. Among them, the value of n is 1/2 for the direct transition and 2 for the indirect transition. For $Bi_2O_2CO_3$ and pure g-$C_3N_4$, the values of n are 1/2 and 2, respectively (Wang *et al.* 2010; Zhao *et al.* 2015). As is shown in Figure 5(b) and 5(c), the band gap values of g-CN, BiOC(2.0)/g-CN and $Bi_2O_2CO_3$ are estimated to 2.63 eV, 2.40 eV and 3.26 eV, respectively. In a similar manner, the band gaps of BiOC(0.5)/g-CN and BiOC(1.5)/g-CN are 2.43 eV and 2.36 eV. Additionally, the potentials of the valence band (VB) and conduction band (CB) of a semiconductor material can be calculated by the following equations (Zhao *et al.* 2012; Chen *et al.* 2015):

$$E_{VB} = X - E^e + 0.5Eg \quad (1)$$

$$E_{CB} = E_{VB} - Eg \quad (2)$$

where $E_{VB}$ is the valence band edge potential; X is the electronegativity of the semiconductor, and the X values of g-CN and $Bi_2O_2CO_3$ are 4.67 eV and 6.54 eV, respectively (Ma *et al.* 2017a, 2017b). $E^e$ is the energy of free electrons vs. the hydrogen scale (about 4.5 eV . NHE); and Eg is the band gap energy of the semiconductor. The band gap energies of g-CN and $Bi_2O_2CO_3$ are adopted as 2.63 eV and

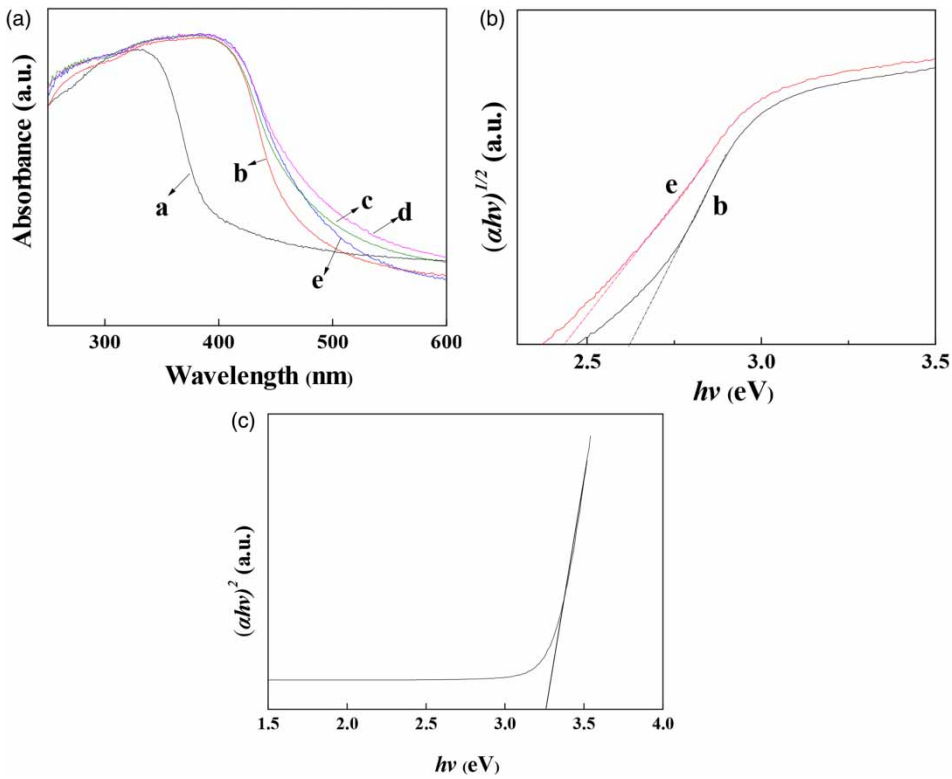


**Figure 5** | (a) The diffuse reflectance spectra for different catalyst samples (a) $Bi_2O_2CO_3$, (b) g-CN, (c) BiOC (0.5)/g-CN, (d) BiOC (1.5)/g-CN and (e) BiOC (2.0)/g-CN; (b) Tauc plots for (b) g-CN and (e) BiOC (2.0)/g-CN; (c) Tauc plot for $Bi_2O_2CO_3$.

3.26 eV, respectively. The positions of the conduction band and valence band of g-CN and $Bi_2O_2CO_3$ can be calculated by Equations (1) and (2), which the $E_{VB}$, $E_{CB}$ of g-CN and $Bi_2O_2CO_3$ are 1.49 eV/NHE, −1.14 eV/NHE and 3.77 eV/NHE, 0.51 eV/NHE, respectively.

The photocatalytic degradation of TC under the visible light irradiation was used as a test reaction to evaluate the catalytic properties of the various BiOC/g-CN samples. As shown in Figure 6(a), without the presence of any photocatalyst, the degradation efficiency of TC is very low, which eliminates the possibility of a self-photolysis process. Among these catalysts, g-CN exhibits the poorest catalytic activity, due to fast charge-carrier recombination. Moreover, BiOC/g-CN composites show more enhanced activity in the degradation of TC relative to the g-CN sample. The maximum degradation efficiency of 98.1% is attained for BiOC(1.5)/g-CN composite.

Following a Langmuir–Hinshelwood kinetic model, the photocatalytic degradation reaction of TC over photocatalysts is expressed by the pseudo first-order equation at low

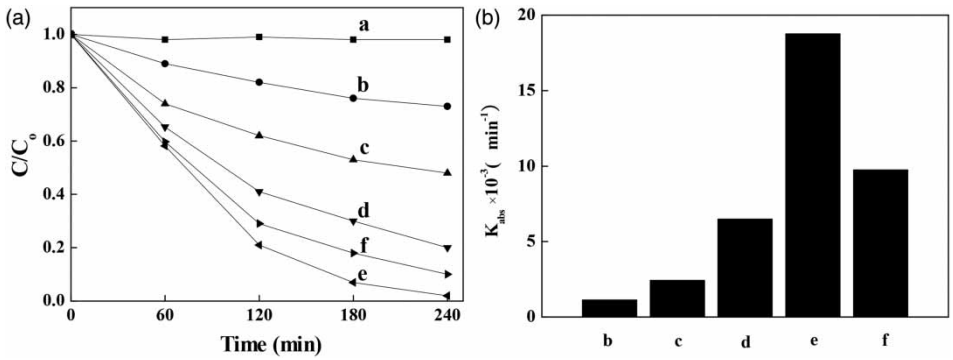


**Figure 6** | (a) Photocatalytic degradation of TC under visible light irradiation using various catalysts: (a) no catalysts, (b) g-CN, (c) BiOC(0.5)/g-CN, (d) BiOC(1.0)/g-CN, (e) BiOC (1.5)/g-CN, and (f) BiOC(2.0)/g-CN; (b) the degradation rate constant of TC over various catalysts: (b) g-CN, (c) BiOC (0.5)/g-CN, (d) BiOC (1.0)/g-CN, (e) BiOC(1.5)/g-CN, and (f) BiOC(2.0)/g-CN.

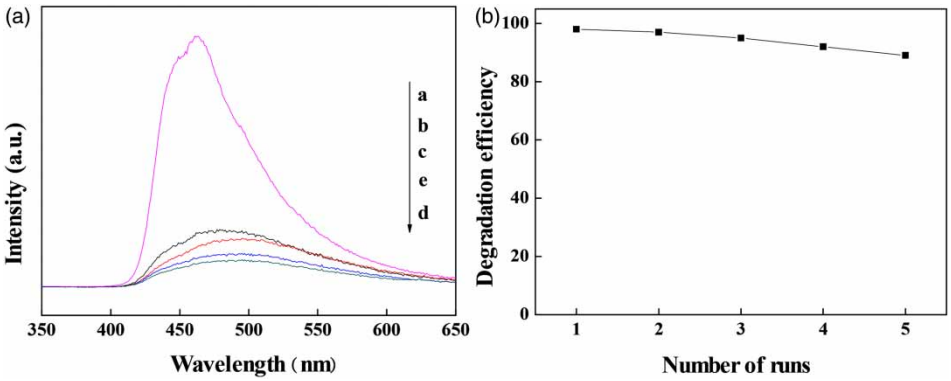


**Figure 7** | (a) PL spectra of different samples: (a) g-CN, (b) BiOC (0.5)/g-CN, (c) BiOC (1.0)/g-CN, (d) BiOC (1.5)/g-CN, (e) BiOC (2.0)/g-CN; (b) stability test for the photocatalytic degradation of TC over BiOC(1.5)/g-CN.

concentrations: $ln(Co/C) = kt$, where $t$ is the irradiation time and $k$ is the rate constant (Pirhashemi & Habibi-Yangjeh 2013). The photocatalytic degradation kinetics of TC have been investigated and the obtained results are shown in Figure 6(b). The degradation rate constant of TC over the g-CN is $1.1 \times 10^{-3}$ $min^{-1}$, and the significantly enhanced activity is observed for the degradation reaction over the BiOC/g-CN nanocomposites. The activity of the best nanocomposite, BiOC(1.5)/g-CN, with a rate constant of $18.7 \times 10^{-3}$ $min^{-1}$ is nearly 16.7 times greater than that of the g-CN sample.

To uncover the improved activity of the composites relative to the pristine sample, PL spectra were provided to show the separation efficiency of electron–hole pairs and the results for the different samples are shown in Figure 7(a). The strong PL intensity of g-CN implies that the electrons and holes recombine fast. By comparison with g-CN, the BiOC/g-CN composites have drastic quenching of PL intensities, and BiOC (1.5)/g-CN has the lowest intensity in its spectrum. In generally, the lower intensity indicates the decrease in the recombination of the photogenerated charge carriers (Hong *et al.* 2017; Duan *et al.* 2018). Therefore, the heterostructured BiOC/g-CN is highly favorable for efficient separation of photoinduced charge carriers, which is helpful for improvement of photocatalytic reaction.

The stability of the composite catalyst was investigated by performing recycle experiments with BiOC(1.5)/g-CN catalyst under visible light irradiation (Figure 7(b)). The catalyst shows very little variation in activity even after five cycles, demonstrating that it has high stability. All these results suggest that BiOC/g-CN composites are promising visible light catalysts for actual application.

The excellent photocatalytic performance of BiOC/g-CN composite is owing to both an increase in the surface area of the catalyst and the formation of the heterojunction between $Bi_2O_2CO_3$ and g-$C_3N_4$, which can effectively enhance the absorption of visible light and facilitate the separation of photo-induced carriers. BiOC(1.5)/g-CN and BiOC(0.5)/g-CN have similar BET surface area (26.01 and 22.01 $m^2$/g), and similar diffuse reflectance spectra. The $k_{abs}$ of BiOC(1.5)/g-CN is about 7 times higher than that of BiOC(0.5)/g-CN. This result indicates that both surface area and absorption of visible light are not major factors that contribute to the BiOC(1.5)/g-CN catalyst's enhanced photocatalytic performance. It can be observed that the amount of $Bi_2O_2CO_3$ is a crucial factor for enhancing the photocatalytic properties of BiOC/g-CN composites. By using an appropriate mass ratio, an efficient heterojunction between $Bi_2O_2CO_3$ and g-$C_3N_4$ could be formed, which can effectively restrain the recombination of photogenerated charges, dramatically improving the photocatalytic properties (Zuo *et al.* 2018). At a low amount of $Bi_2O_2CO_3$ (0.5 wt%, 1.0 wt%), the utilization of $Bi_2O_2CO_3$ for photocatalytic performance was lower, and thus a lower degradation efficiency was observed, whereas a higher amount of $Bi_2O_2CO_3$ (2.0 wt%) may lead to agglomeration of bismuth species, resulting in lower activity towards the degradation of TC.

The possible mechanism for the photocatalytic degradation of TC over BiOC/g-CN composites is displayed in Figure 8. When the TC suspension containing a certain quantity of BOC/CN catalysts is exposed to visible light ($\lambda > 420$ nm), the VB of g-CN nanosheets with proper Eg (2.63 eV) can be excited to its CB while there is no response about the VB of $Bi_2O_2CO_3$ in the heterostructure due to its wide Eg (3.26 eV). Yet, in the BOC/g-CN composites, the $E_{CB}$ of g-$C_3N_4$ (1.49 eV/NHE) is more negative than that of $Bi_2O_2CO_3$ (3.77 eV/NHE), the electrons in the conduction band of g-$C_3N_4$ can easily migrate to the conduction band of $Bi_2O_2CO_3$ due to the interfacial interactions

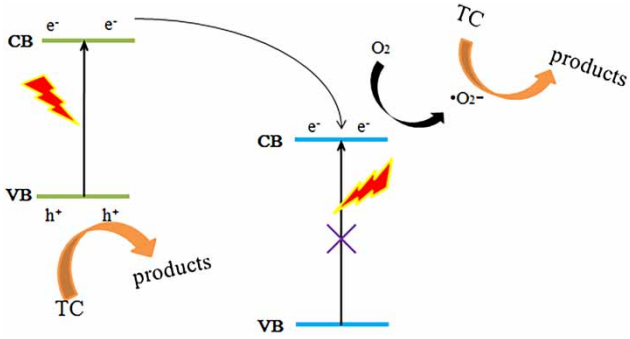


**Figure 8** | Proposed possible reaction mechanism for the photocatalytic degradation of TC.

between two components (Zheng & Jiao 2017). Thus, the electron-hole recombination can be effectively suppressed, which explains the promotion for the degradation process.

## CONCLUSIONS

In sum, we successfully fabricated a series of $Bi_2O_2CO_3$/g-$C_3N_4$ composites with different $Bi_2O_2CO_3$ content by a simple one-pot synthetic strategy. The $Bi_2O_2CO_3$/g-$C_3N_4$ composites showed much higher photocatalytic degradation ability for TC than the pristine g-$C_3N_4$ material under visible light, and the photocatalytic activity would achieve its maximum when the weight content of $Bi_2O_2CO_3$ was 1.5%. Moreover, the $Bi_2O_2CO_3$/g-$C_3N_4$ composites exhibited excellent reaction stability in the recycling experiment, which was vital for practical applications. The improved photocatalytic activity was attributed to the large surface area of g-$C_3N_4$ nanosheets and the heterojunction between $Bi_2O_2CO_3$ and g-$C_3N_4$, which could facilitate the separation of photogenerated electron-hole pairs.

## ACKNOWLEDGEMENTS

The authors are grateful to the Chinese National Foundation of Natural Sciences (Grant No. 21276027, 21507006, 21476171 and 51808040); Shandong Provincial Natural Science Foundation (ZR2014BL018, ZR2015BL018 and 2016BL28); Shandong Province college science and technology plan project (J16LC58, 17KB001, 18KA013 and18KB058); Key Research and Development Plan Project of Shandong Province (2015GGX104012, 2017GGX80104) and Foundation of Binzhou University (2014Y08, 2015ZDL02, BZXYG1708, and BZXYG1709) for financial support.

## REFERENCES

Akhundi, A. & Habibi-Yangjeh, A. 2017 Graphitic carbon nitride nanosheets decorated with $CuCr_2O_4$ nanoparticles: novel photocatalysts with high performances in visible light degradation of water pollutants. *J. Colloid. Interf. Sci.* **504**, 697–710.

Bai, X., Sun, C., Liu, D., Luo, X., Li, D., Wang, J., Wang, N., Chang, X. & Zhu, Y. 2017 Photocatalytic degradation of deoxynivalenol using graphene/ZnO hybrids in aqueous suspension. *Appl. Catal. B: Environ.* **204**, 11–20.

Chen, Y., Wang, B., Lin, S., Zhang, Y. & Wang, X. 2014 Activation of n → π* transitions in two-dimensional conjugated polymers for visible light photocatalysis. *J. Phys. Chem. C.* **118**, 29981–29989.

Chen, X., Zhou, B., Yang, S., Wu, H., Wu, Y., Wu, L., Pan, J. & Xiong, X. 2015 In situ construction of an $SnO_2$/g-$C_3N_4$ heterojunction for enhanced visible-light photocatalytic activity. *RSC Adv.* **5**, 68953–68963.

Dong, F., Wu, L., Sun, Y., Fu, M., Wu, Z. & Lee, S. C. 2011 Efficient synthesis of polymeric g-$C_3N_4$ layered materials as novel efficient visible light driven photocatalysts. *J. Mater. Chem.* **21**, 15171–15174.

Dong, F., Zhao, Z., Xiong, T., Ni, Z., Zhang, W., Sun, Y. & Ho, W. 2013 In situ construction of g-$C_3N_4$/g-$C_3N_4$ metal-free heterojunction for enhanced visible-light photocatalysis. *ACS Appl. Mater. Interfaces.* **5**, 11392–11401.

Duan, Y. & Shen, Y. 2017 Synthesis of ZnO-CuO/MCM-48 photocatalyst for the degradation of organic pollutions. *Water. Sci. Technol.* **76**, 172–181.

Duan, Y., Zhai, D., Zhang, X., Zheng, J. & Li, C. 2018 Synthesis of CuO/Ti-MCM-48 photocatalyst for the degradation of organic pollutions under solar-simulated irradiation. *Catal. Lett.* **148**, 51–61.

Hong, Y., Li, C., Fang, Z., Luo, B. & Shi, W. 2017 Rational synthesis of ultrathin graphitic carbon nitride nanosheets for efficient photocatalytic hydrogen evolution. *Carbon* **121**, 463–471.

Jiang, G., Wang, X., Wei, Z., Li, X., Xi, X., Hu, R., Tang, B., Wang, R., Wang, S., Wang, T. & Chen, W. 2013 Photocatalytic properties of hierarchical structures based on Fe-doped BiOBr hollow microspheres. *J. Mater. Chem. A* **1**, 2406–2410.

Jiang, W., Luo, W., Zong, R., Yao, W., Li, Z. & Zhu, Y. 2016 Polyaniline/carbon nitride nanosheets composite hydrogel: a separation-free and high-efficient photocatalyst with 3d hierarchical structure. *Small* **12**, 4370–4378.

Li, Y., Zhan, J., Huang, L., Xu, H., Li, H., Zhang, R. & Wu, S. 2014 Synthesis and photocatalytic activity of a bentonite/g-$C_3N_4$ composite. *RSC Adv.* **4**, 11831–11839.

Li, Y., Wu, S., Huang, L., Xu, H., Zhang, R., Qu, M., Gao, Q. & Li, H. 2015 g-$C_3N_4$ modified $Bi_2O_3$ composites with enhanced visible-light photocatalytic activity. *J. Phys. Chem. Solids* **76**, 112–119.

Liang, N., Wang, M., Jin, L., Huang, S., Chen, W., Xu, M., He, Q., Zai, J., Fang, N. & Qian, X. 2014 Highly efficient $Ag_2O$/$Bi_2O_2CO_3$ p-n heterojunction photocatalysts with improved visible-light responsive activity. *ACS Appl. Mater. Inter.* **6**, 11698–11705.

Lin, Q., Li, L., Liang, S., Liu, M., Bi, J. & Wu, L. 2015 Efficient synthesis of monolayer carbon nitride 2D nanosheet with tunable concentration and enhanced visible-light photocatalytic activities. *Appl. Catal. B: Environ.* **163**, 135–142.

Luo, L., Zhang, A., Janik, M. J., Li, K., Song, C. & Guo, X. 2017 Inorganic salt-assisted fabrication of graphitic carbon nitride with enhanced photocatalytic degradation of Rhodamine B. *Mater. Lett.* **188**, 130–133.

Ma, P., Yu, Y., Xie, J. & Fu, Z. 2017a $Ag_3PO_4$/CuO composites utilizing the synergistic effect of photocatalysis and Fenton-like catalysis to dispose organic pollutants. *Adv. Powder. Technol.* **28**, 2797–2804.

Ma, Y., Bian, Y., Tan, P., Shang, Y., Liu, Y., Wu, L., Zhu, A., Liu, W., Xiong, X. & Pan, J. 2017b Simple and facile ultrasound-assisted fabrication of $Bi_2O_2CO_3$/g-$C_3N_4$ composites with excellent photoactivity. *J. Colloid. Interf. Sci.* **497**, 144–154.

Mamba, G. & Mishra, A. K. 2016 Graphitic carbon nitride (g-$C_3N_4$) nanocomposites: a new and exciting generation of visible light driven photocatalysts for environmental pollution remediation. *Appl. Catal. B: Environ.* **198**, 347–377.

Panneri, S., Ganguly, P., Nair, B., Mohamed, A., Warrier, K. & Hareesh, U. 2016 Copyrolysed $C_3N_4$-Ag/ZnO ternary heterostructure systems for enhanced adsorption and photocatalytic degradation of tetracycline. *Eur. J. Inorg. Chem.* **2016**, 5068–5076.

Pirhashemi, M. & Habibi-Yangjeh, A. 2013 Simple and large scale one-pot method for preparation of AgBr–ZnO nanocomposites as highly efficient visible light photocatalyst. *Appl. Surf. Sci.* **283**, 1080–1088.

Rong, J., Zhang, T., Qiu, F. & Zhu, Y. 2017 Preparation of efficient, stable, and reusable laccase–$Cu_3(PO_4)_2$ hybrid microspheres based on copper foil for decoloration of Congo red. *ACS Sustain. Chem. Eng.* **5**, 4468–4477.

Shinde, S., Sami, A. & Lee, J. 2016 Sulfur mediated graphitic carbon nitride/S-Se-graphene as a metal-free hybrid photocatalyst for pollutant degradation and water splitting. *Carbon* **96**, 929–936.

Tian, N., Huang, H., Guo, Y., He, Y. & Zhang, Y. 2014 A g-$C_3N_4$/$Bi_2O_2CO_3$ composite with high visible-light-driven photocatalytic activity for rhodamine B degradation. *Appl. Surf. Sci.* **322**, 249–254.

Wang, X., Maeda, K., Thomas, A., Takanabe, K., Xin, G., Carlsson, J. M., Domen, K. & Antonietti, M. 2009 A metal-free polymeric photocatalyst for hydrogen production from water under visible light. *Nat. Mater.* **8**, 76–80.

Wang, Y., Di, Y., Antonietti, M., Li, H., Chen, X. & Wang, X. 2010 Excellent visible-light photocatalysis of fluorinated polymeric carbon nitride solids. *Chem. Mater.* **22**, 5119–5121.

Wang, L., Wang, C., Hu, X., Xue, H. & Pang, H. 2016 Metal/graphitic carbon nitride composites: synthesis, structures, and applications. *Chem.–An. Asian. J.* **11**, 3305–3328.

Wu, M., Yan, J., Zhang, X. & Zhao, M. 2015 Synthesis of g-$C_3N_4$ with heating acetic acid treated melamine and its photocatalytic activity for hydrogen evolution. *Appl. Surf. Sci.* **354**, 196–200.

Xiong, M., Chen, L., Yuan, Q., He, J., Luo, S., Au, C. & Yin, S. 2014 Facile fabrication and enhanced photosensitized degradation performance of the g-$C_3N_4$–$Bi_2O_2CO_3$ composite. *Dalton Trans.* **43**, 8331–8337.

Yan, J., Zhou, C., Li, P., Chen, B., Zhang, S., Dong, X., Xi, F. & Liu, J. 2016 Nitrogen-rich graphitic carbon nitride: controllable nanosheet-like morphology, enhanced visible light absorption and superior photocatalytic performance. *Colloid. Surface. A.* **5**, 257–264.

Yang, M., Hu, S., Li, F., Fan, Z., Wang, F., Liu, D. & Gui, J. 2014 The influence of preparation method on the photocatalytic performance of g-$C_3N_4$/$WO_3$ composite photocatalyst. *Ceram. Int.* **40**, 11963–11969.

Zhang, X., Xie, X., Wang, H., Zhang, J., Pan, B. & Xie, Y. 2012 Enhanced photoresponsive ultrathin graphitic-phase $C_3N_4$ nanosheets for bioimaging. *J. Am. Chem. Soc.* **135**, 18–21.

Zhang, H., Guo, L., Zhao, L., Wan, B. & Yang, Y. 2015a Switching oxygen reduction pathway by exfoliating graphitic carbon nitride for enhanced photocatalytic phenol degradation. *J. Phys. Chem. Lett.* **6**, 958–963, 347–377.

Zhang, Q., Wang, H., Hu, S., Lu, G., Bai, J., Kang, X., Liu, D. & Gui, J. 2015b Synthesis and properties of visible light responsive g-$C_3N_4$/$Bi_2O_2CO_3$ layered heterojunction nanocomposites. *RSC Adv.* **5**, 42736–42743.

Zhao, W., Wang, Y., Yang, Y., Tang, J. & Yang, Y. 2012 Carbon spheres supported visible-light-driven CuO-$BiVO_4$ heterojunction: preparation, characterization, and photocatalytic properties. *Appl. Catal. B: Environ.* **115–116**, 90–99.

Zhao, W., Wei, Z., He, H., Xu, J., Li, J., Yang, S. & Sun, C. 2015 Supporting 1-D $AgVO_3$ nanoribbons on single layer 2-D graphitic carbon nitride ultrathin nanosheets and their excellent photocatalytic activities. *Appl. Catal. A: Gen.* **501**, 74–82.

Zheng, J. & Jiao, Z. 2017 Magnetic recyclable bismuth oxyiodide/polyacrylic anion exchange resin composites with enhanced photocatalytic activity under visible light. *J. Colloid. Interf. Sci.* **504**, 620–625.

Zuo, S., Xu, H., Liao, W., Yuan, X., Sun, L., Li, Q., Zan, J., Li, D. & Xia, D. 2018 Molten-salt synthesis of g-$C_3N_4$-$Cu_2O$ heterojunctions with highly enhanced photocatalytic performance. *Colloids Surf. A Physicochem. Eng. Asp.* **546**, 307–315.

First received 25 August 2018; accepted in revised form 15 April 2019. Available online 23 April 2019